Petroleum Science 22 (2025) 5128–5141

Contents lists available at ScienceDirect

Petroleum Science

journal homepage: www.keaipublishing.com/en/journals/petroleum-science

Original Paper

# Multifactor controls on imbibition oil recovery in shale: Insights from low-field nuclear magnetic resonance

Qi Lv [a,b], Jian Hou [a,*], Ting Chen [b], Yan-Feng Ji [b], Jing Lv [b], Jian-Xun Chen [b]

[a] School of Petroleum Engineering, China University of Petroleum (East China), Qingdao, 266580, Shandong, China
[b] Exploration and Development Research Institute of Shengli Oilfield Company, Sinopec, Dongying, 257015, Shandong, China

ARTICLE INFO

*Article history:*
Received 30 June 2025
Received in revised form
28 July 2025
Accepted 19 October 2025
Available online 1 November 2025

Edited by Meng-Jiao Zhou

*Keywords:*
Shale oil
Jiyang Depression
Imbibition
Nuclear magnetic resonance
Recovery efficiency

ABSTRACT

Shale is characterized by a complex mineral composition and a well-developed, multiscale pore network spanning from micropores to nanopores, which gives rise to a highly intricate microscopic imbibition mechanism. Utilizing shale samples from the Jiyang Depression, experiments are conducted to systematically examine the influence of lithofacies, fluid type, fracture density, wettability, and fluid viscosity on the spontaneous imbibition behavior of shale. Low-field nuclear magnetic resonance serves as the principal analytical method for investigating fluid migration dynamics and spatial distribution within the multiscale pore structure of shale. The results indicate that, at the microscopic scale, imbibition-driven oil recovery is primarily controlled by capillary forces, which must overcome various forms of resistance to effectively displace oil with water. For massive cores without fracture, oil recovery is primarily contributed by nanopores within the matrix. In contrast, cores containing laminations and natural fractures preferentially mobilize oil from larger pores, as the flow resistance in nanopores is significantly greater than that in micropores. Transverse relaxation time spectrum from nuclear magnetic resonance further reveals that $CO_2$, compared to water, can mobilize more oil from large pores via molecular diffusion. However, water exhibits superior displacement efficiency in smaller pores. Hydrophilic cores demonstrate the highest imbibition efficiency, and the addition of imbibition enhancers further improves displacement performance. On the other hand, increasing fluid viscosity suppresses both the imbibition-driven displacement process and overall fluid mobility.


## 1. Introduction

Shale oil, as a significant field of unconventional hydrocarbon exploration and development, plays a crucial role in ensuring national energy security (Zou et al., 2013; Bai et al., 2025). Following over five decades of sustained research and exploration, shale oil in the United States has successively built major shale oil and gas production areas such as Bakken and Eagle Ford (Pranesh, 2018; Wang et al., 2020; Xiao et al., 2023), demonstrating the enormous resource potential of shale oil and gas. China has obtained industrial oil flow in Ordos Basin, Junggar Basin, Songliao Basin, Bohai Bay Basin, Jiyang Depression, etc. (Zou et al., 2018; Sun et al., 2022; Zhang et al., 2022), and has successively established three national shale oil demonstration areas in Jimsar, Daqing Gulong, and Shengli Jiyang. Shale oil has gradually become an important national energy replacement position.

In contrast to the relatively stable marine shale formations of North America, continental fine-grained sedimentary shales in China exhibit extremely low porosity and permeability, pronounced heterogeneity, and substantial variation in oil content (Tang et al., 2019; Yan et al., 2021; Wang et al., 2024). After the creation of complex fracture networks through reservoir stimulation, fracturing fluid can displace shale oil in the matrix by high pressure gradient and imbibition, thereby increasing the estimated ultimate recovery of a single well. An extensive indoor experiments and numerical simulations on the imbibition in unconventional oil and gas reservoirs have been conducted. The pore structure, fluid properties, and their interactions are the main factors affecting the imbibition of shale reservoirs (Kibria et al., 2018; Cai et al., 2021; Wang et al., 2023; Yang et al., 2023b). The

* Corresponding author.
*E-mail address:* sllx_upc@126.com (J. Hou).
Peer review under the responsibility of China University of Petroleum (Beijing).

https://doi.org/10.1016/j.petsci.2025.10.019

presence of multiscale micro/nanopores and diverse mineral compositions in shale reservoirs leads to highly complex interaction mechanisms between the fracturing fluid and the shale matrix.

For imbibition experiments, there are direct weighing method, indirect method, and volumetric method (Ghanbari and Dehghanpour, 2015; Cai et al., 2020; Li et al., 2023), which mainly focus on analyzing the influence of shale mineral composition (Yang et al., 2019), micro pore structure (Cai et al., 2025), wettability (Tangparitkul et al., 2023) and other factors on imbibition. Previous studies have used CT scanning (Zhao et al., 2019; Han et al., 2025), scanning electron microscopy (Liu et al., 2024), nuclear magnetic resonance (Wei et al., 2024), low-pressure $CO_2$/$N_2$ adsorption (Zhang, 2016) and other methods to qualitatively analyze the effect of water imbibition on micro pore structure of shale. In the imbibition experiments of water and surfactant solutions, Roychaudhuri et al. (2013) observed an obvious transition of imbibition rate from linearly depending on the square root of time to a lower rate at later times. Gao and Hu (2016) conducted spontaneous imbibition experiments on Barnett shale and discovered spontaneous imbibition could be affected by the initial water saturation and mineral compositions, especially clay content. The driving pressure of fracturing fluids and the high salinity of formation fluids both significantly influence the overall imbibition process. Shao et al. (2024) found that salinity and driving pressure have notable effects on water imbibition and proposed a modified Handy model that effectively characterizes the forced imbibition behavior of shale. Guo et al. (2020) conducted experiments on Ordos Basin cores and concluded that a higher permeability of the core has a larger imbibition recovery. Ma et al. (2022) discovered that the imbibition ability of coal samples becomes worse with the increase of the confining pressure. Further, the effects of salt solutions surfactant and ion diffusion on spontaneous imbibition were investigated by Yang et al. (2023a), which revealed that the imbibition rate of shale is the slowest compared with sandstone and hydrate sediment in distilled water. In general, most imbibition experiments are conducted under ambient temperature and atmospheric pressure conditions. However, shale in subsurface reservoirs is subjected to elevated temperatures and in-situ stresses, making conventional experimental approaches insufficient to accurately capture its true imbibition behavior.

Compared to other methods, low-field nuclear magnetic resonance (LF-NMR) technology offers significant advantages in characterizing imbibition behavior. It not only directly reveals fluid distribution within core pores, but also enables quantitative evaluation of oil recovery across different pore size ranges. In contrast to high-field NMR, LF-NMR operates at a significantly lower magnetic field strength (typically between 0.01 and 0.5 T). Due to the strong magnetic susceptibility heterogeneity in rock samples, high-field NMR is prone to severe image distortions and signal artifacts. In contrast, LF-NMR has the advantages of short measurement time, high accuracy, and non-destructive sample (Xia et al., 2024). Nie and Chen (2018) employed LF-NMR techniques to monitor the dynamic distribution of oil and water during the spontaneous imbibition process. Their results showed that water preferentially invades micropores and mesopores due to the strong capillary forces within these pore scales. As a result, oil originally present in the micropores and mesopores is displaced into connected macropores, while the oil initially residing in the macropores is subsequently expelled. Furthermore, LF-NMR imaging revealed that, with increasing imbibition time, the remaining oil tends to accumulate in the central region of the core and becomes surrounded by the invading water phase. Gu et al. (2017) conducted spontaneous imbibition experiments on the low-permeability sandstone reservoirs of the Yanchang Formation using a combination of LF-NMR and computed CT. Their study investigated the effect of permeability on imbibition recovery and concluded that higher matrix permeability leads to an exponential increase in connected pore throats, which in turn enhances spontaneous imbibition recovery efficiency.

Although previous studies have made progress in understanding imbibition behavior in shale reservoirs, research on the imbibition characteristics of different lithofacies in the Jiyang Depression remains limited. The variations in pore structure and wettability among these lithofacies present significant challenges to comprehensively elucidating the underlying imbibition mechanisms. Therefore, in this study, a series of imbibition experiments is conducted on shales from the Jiyang Depression using LF-NMR techniques. The influence of lithofacies, type of fluids, fracture density, core wettability, and fluid viscosity on imbibition behavior and oil recovery is systematically evaluated. The contribution of pores of varying sizes is quantified, and the roles of lamination and natural fractures in enhancing capillary-driven flow are specifically analyzed. The relationship between fracture-induced surface area growth and imbibition performance is established, and wettability is identified as a key factor controlling the direction and intensity of capillary forces. The results provide a detailed understanding of the microscopic mechanisms governing shale imbibition and offer valuable guidance for selecting appropriate fracturing fluids and designing effective stimulation strategies in low-permeability shale oil reservoirs.

## 2. Samples and methodology

### 2.1. Samples

The shale samples used in this study were collected from the Niuzhuang, Pingnan, Boxing, and Minfeng sags, at depths ranging from 3277.65 to 3794.55 m. Most samples are from the fourth member of the Shahejie Formation, with a few from the third member. Permeability was measured using the pulse decay method and ranges from $0.01 \times 10^{-3}$ to $10.7 \times 10^{-3}$ μm$^2$. Porosity was determined using nitrogen gas based on Boyle law, with values ranging from 1.12% to 13.40%. Detailed petrophysical properties of the shale samples are summarized in Table 1.

### 2.2. Methodology

#### 2.2.1. LF-NMR

During an NMR phenomenon, a relaxation process occurs, which is closely related to the pore structure. Generally, hydrogen-containing fluids in the pore space (e.g., water and oil) exhibit three transverse relaxation mechanisms: bulk relaxation, surface relaxation, and diffusion relaxation. Since these mechanisms are independent of each other, the total transverse relaxation time ($T_2$) can be expressed as:

$$\frac{1}{T_2}=\frac{1}{T_{2B}}+\frac{1}{T_{2S}}+\frac{1}{T_{2D}} \tag{1}$$

where $T_{2B}$ represents bulk relaxation, $T_{2S}$ represents surface relaxation, and $T_{2D}$ represents diffusion relaxation. Since none of the experiments conducted in this study involve a gradient magnetic field, diffusion relaxation can be neglected. Generally, for water in sandstone pores, the timescale of bulk relaxation (typically around 3 s) is significantly longer than that of surface relaxation (usually a few hundred milliseconds). According to Eq. (1), the influence of bulk relaxation can be disregarded. Therefore, in the relaxation process within porous media, surface relaxation dominates, and the total transverse relaxation time $T_2$ can be

**Table 1**
Petrophysical properties of collected shales.

| Well | No. | Depth, m | Lithology | Length, cm | Diameter, cm | Porosity, % | Permeability, $10^{-3}$ μm$^2$ |
|---|---|---|---|---|---|---|---|
| N55-X1 | 7 | 3335.80 | CL | 2.44 | 2.48 | 2.19 | 0.06 |
| | 25 | 3345.25 | LCIL | 2.40 | 2.51 | 2.03 | 3.15 |
| | 40 | 3358.30 | LCIL | 2.36 | 2.51 | 1.12 | 0.01 |
| | 59 | 3452.70 | M | 2.57 | 2.47 | 1.46 | 0.22 |
| | 66 | 3458.43 | LBCIL | 2.57 | 2.44 | / | / |
| | 70 | 3465.62 | LBCIL | 2.54 | 2.42 | / | / |
| | 73 | 3538.80 | LCIL | 2.50 | 2.50 | 5.92 | 1.87 |
| | 113 | 3590.45 | FT | 2.52 | 2.48 | 7.36 | 1.73 |
| | 133 | 3609.05 | BCLS | 2.56 | 2.42 | 4.38 | 4.62 |
| B172 | A | 3277.65 | / | 8.06 | 11.88 | / | / |
| | B | | | 11.54 | 11.80 | | |
| FY1 | 1 | 3450.60 | / | 2.50 | 2.50 | / | / |
| FY1-1HF | 11 | 3578.10 | L | 2.50 | 2.50 | 8.10 | 10.70 |
| | 34 | 3603.02 | L | 2.50 | 2.50 | 5.20 | 1.17 |
| | 49 | 3610.92 | L | 2.50 | 2.50 | 11.10 | 2.42 |
| | 66 | 3619.72 | L | 2.50 | 2.50 | 4.60 | 10.60 |
| | 84 | 3628.93 | L | 2.50 | 2.50 | 9.70 | 8.39 |
| | 191 | 3674.55 | LCCFS | 2.50 | 2.50 | / | / |
| | 126 | 3794.55 | L | 2.50 | 2.50 | 13.40 | 5.56 |

Note: CL—cryptocrystalline lamination; LCIL—laminated cryptocrystalline interbedded layers; M-massive; LBCIL—laminated bright crystalline interbedded layers; FT—fracture type; BCLS—bright crystalline laminated shale; L—lamination; LCCFS—laminated cryptocrystalline calcareous-felsic shale.

approximated as the surface relaxation time $T_{2S}$. The surface relaxation process is governed by the properties of the solid-liquid interface and the characteristics of the pore space. Consequently, the transverse relaxation time can be described in terms of the pore surface area and pore volume:

$$\frac{1}{T_2}=\frac{1}{T_{2S}}=\rho\frac{S}{V}=\rho\frac{F}{R} \tag{2}$$

where $\rho$ represents the surface relaxation rate, $S$ denotes the pore surface area, and $V$ represents the pore volume. $F$ is the shape factor, where $F=1$ corresponds to a planar geometry, $F=2$ to a cylindrical shape, and $F=3$ to a spherical shape. $R$ denotes the pore radius. Based on Eq. (2), the conversion relationship between pore radius and transverse relaxation time can be obtained:

$$R=\rho F T_2 \tag{3}$$

### 2.2.2. Wettability

Shale wettability is a critical factor influencing the imbibition process. Wettability tests are conducted on four types of microcrystalline shale from the N55-X1, FYP1, and FY1-1HF wells in the Jiyang Depression. According to the "Methods for Determining Reservoir Rock Wettability", shale samples are saturated with kerosene and sequentially subjected to spontaneous water imbibition, water flooding, spontaneous oil imbibition, and oil flooding. During each stage, $T_2$ spectra are measured, and the changes in the $T_2$ spectra are used to calculate the volumes of spontaneous water imbibition, water-flooded oil displacement, spontaneous oil imbibition, and oil-flooded water displacement. The wettability of each core samples is calculated using Eqs. (4)–(6), as shown in Table 2. The comprehensive wettability index for the N55-X1 core is −0.58, indicating an oil-wet core; the comprehensive wettability index for the N55-X1 core is −0.04, indicating a neutral core; the comprehensive wettability index for the FYP1 core is 0.36, indicating a water-wet core; and the comprehensive wettability index for the FY1-1HF core is 0.4, indicating a water-wet core.

**Table 2**
Wettability of different pores in four kinds of cores.

| Well | No. | $I$-micropores | $I$-macropores | $I$ | Wettability |
|---|---|---|---|---|---|
| N55-X1 | 66 | −0.35 | −0.93 | −0.58 | Oil-wet |
| N55-X1 | 73 | −0.13 | −1.30 | −0.04 | Neutral |
| FYP1 | 1 | 0.02 | 0.42 | 0.36 | Hydrophilic |
| FY1-1HF | 191 | 0.68 | −1.75 | 0.40 | Hydrophilic |

$$W_w=\frac{V_{o1}}{V_{o1}+V_{o2}} \tag{4}$$

$$W_o=\frac{V_{w1}}{V_{w1}+V_{w2}} \tag{5}$$

$$I=W_w-W_o \tag{6}$$

where $W_w$ represents the water-wettability index; $W_o$ represents the oil-wettability index; $V_1$ denotes the volume of spontaneous water imbibition and oil displacement in the core sample; $V_{o2}$ represents the volume of water-flooded oil displacement in the core sample; $V_{w1}$ denotes the volume of spontaneous oil imbibition and water displacement in the core sample; $V_{w2}$ represents the volume of oil-flooded water displacement in the core sample; and $I$ represents the relative wettability index. Based on the $T_2$ spectra and Eq. (2), a pore radius of 0.1 μm is selected as the boundary between micropores and macropores, allowing the wettability index to be determined separately for each pore size category.

## 2.3. Experimental procedures

The LF-NMR analyzer (MacroMR12-150H-I) from the NIUMAG company is utilized in this study. The complete experimental setup includes a displacement pump, intermediate container, NMR equipment, waste fluid collection container, and data acquisition system, as shown in Fig. 1.

(a) Static imbibition experiments under different lithofacies
   1) Shale samples from different lithofacies are cleaned to remove residual oil, dried, and then saturated with kerosene at 25 MPa for three days to ensure full saturation. The $T_2$ spectrum of the saturated shale are then acquired.

2) The saturated shale samples are immersed in deuterium water in a beaker, ensuring complete submersion below the liquid surface.
3) At different imbibition time intervals, the shale samples are extracted, and the corresponding $T_2$ spectra are measured using NMR equipment.

(b) In-situ NMR imbibition experiments on shale

In-situ NMR imbibition experiments are conducted using an online NMR imbibition system. The detailed experimental procedure is as follows.

1) Shale samples are cleaned, dried, and saturated with kerosene. The $T_2$ spectrum of the saturated shale is then obtained.
2) The saturated shale samples are placed in the online NMR imbibition system, where different imbibition media are introduced to investigate their effects on shale imbibition recovery and the mobilization of various pore types.
3) The $T_2$ spectrum of the shale samples is acquired in real-time at different imbibition time intervals.
4) Steps 1 to 3 is repeated to examine the effects of fracture density, wettability, and imbibition fluid viscosity on shale imbibition-driven oil recovery. The experimental parameters designed for each test are shown in Table 3.

## 3. Results

### 3.1. Pore structure variation across lithofacies

The laminated structure is the most prominent and extensively developed sedimentary feature in the Jiyang Depression. The interbedding of calcareous and argillaceous laminae forms the most representative structural characteristic of the Jiyang shale. The diversity of lamination types plays a critical role in controlling the internal heterogeneity and pore distribution within the shale. The shale from Jiyang Depression can be classified into four lithofacies: massive shale, cryptocrystalline laminated shale, bright crystalline laminated shale and fractured shale, as shown in Fig. 2.

The pore structure of shale refers to the geometry, size, distribution, and interconnectedness of the pores and throat networks within the rock. It is a key factor influencing the fluid storage capacity, permeability, and ultimately productivity of oil reservoirs. Smaller pores exert greater surface interactions on the fluid molecules, resulting in shorter relaxation times. Therefore, the $T_2$ spectrum provides insight into the distribution of pores of different sizes.

After evacuating the core sample for 24 h, it is pressurized to 20 MPa and saturated with kerosene. LF-NMR technology is then used to measure the pore structure of four different lithofacies of shale, as shown in Fig. 3. The results indicate that the dominant pore diameter in massive shale is around 8 nm, with this lithofacies primarily consisting of nanometer-scale pores, where the proportion of nanopores exceeds 80%. In cryptocrystalline laminated shale, the predominant pore diameter is also approximately 8 nm. However, in contrast to massive shale, cryptocrystalline laminated shale contains additional pores ranging from 50 nm to 150 nm, with the combined proportion of micro-nano and submicron pores making up around 20%. In bright crystalline laminated shale, although the dominant pore diameter remains around 8 nm, there is a notable increase in pores ranging from 100 to 1000 nm, with submicron pores accounting for approximately 20% of the total. The $T_2$ spectrum of the fractured core exhibits a distinct bimodal distribution, with the left peak centered around 1 nm and the right peak around 400 nm.

### 3.2. Imbibition behavior under varying factors

#### 3.2.1. Lithofacies

Using NMR technique, $T_2$ spectrum distributions of shale samples with different lithofacies are obtained at varying imbibition times, as shown in Fig. 4. Since deuterated water ($D_2O$), which produces no NMR signal, is used as the imbibing fluid, the $T_2$ spectral area of the shale progressively decreases with increasing imbibition time. For massive cores, $T_2$ spectral changes primarily occurred in the 0.01−20 ms, corresponding to matrix-dominated imbibition behavior. The smaller matrix pores exerted stronger capillary forces, causing preferential oil displacement from these pores (Meng et al., 2015). Comparison of $T_2$ spectra at 64 and 333 h revealed similar oil volumes imbibed from the matrix. After 333 h, oil in larger pores (>20 ms) is gradually displaced, with partial migration into smaller pores (Fig. 4(a)) (Xiao et al., 2024). For cryptocrystalline laminated shale, spontaneous imbibition during the first 64 h primarily occurred in mesopores and macropores (10−1000 ms). This is attributed to hydration-induced microcracks, which provided preferential flow pathways for $D_2O$, enabling efficient displacement of oil from macropores. However, the oil content in micropores remained virtually unchanged during this period. After 333 h of imbibition, the primary flow pathways shifted to micropores, with secondary contributions from mesopores to micropores (Fig. 4(b)). Bright crystalline laminated shale exhibited most $T_2$ spectral changes within the first 64 h, with meso-macropores and macropores serving as primary flow channels. By 333 h, minor oil imbibition had occurred in micropores and meso/macropores (Fig. 4(c)). Cores with fractured demonstrated rapid imbibition through macropores and fractures, with nearly complete oil displacement achieved within 64 h. Only minimal oil from micropores was observed after 333 h (Fig. 4(d)). By $T_2$ spectrum area of the saturated state and the $T_2$ spectrum areas at different imbibition moments, the imbibition recovery at different imbibition moments can be obtained (Fig. 4(e)). For the four types of lithofacies, as the imbibition time increases, the imbibition rate gradually decreases and eventually approaches equilibrium. The durations to achieve imbibition equilibrium for massive shale, cryptocrystalline laminated shale, bright crystalline laminated shale, and fractured shale are 183, 524, 524, and 333 h respectively. When imbibition reaches equilibrium, the imbibition recovery of different lithofacies types are as follows: fractured shale (24.6%) > bright crystalline laminated shale (22.8%) > cryptocrystalline laminae shale (21.2%) > massive shale (17.9%).

Based on the correspondence between the $T_2$ in nuclear magnetic resonance and pore size, pores are classified into four types: nanopores (<0.05 μm), micro-nanopores (0.05–0.1 μm), submicropores (0.1–1 μm), and micropores (>1 μm) (Chen et al., 2018a, 2018b). The contribution of different pore types to the imbibition equilibrium recovery efficiency is shown in Fig. 5(b). By comparing the proportion of recovery degrees in pore sizes of the four lithofacies cores, it can be found that the higher the proportion of fractures in the core, the higher the imbibition recovery degree. For massive shales, cryptocrystalline laminated cores, and bright crystalline laminated shale, nanopores are the main oil-supplying pores. For fractured cores, micropores serve as the main oil-supplying pores, followed by nanopores. The imbibition behavior of shale in different pores at various imbibition times is shown in Fig. 5(c)–(f). At the micro-scale, oil extraction from shale relies on capillary forces to overcome various resistances, resulting in oil-water displacement. For nearly crack-free massive cores, oil is primarily supplied by the nanopores in the matrix during the initial stages of imbibition and continues to do so until the process is completed. In contrast, for cryptocrystalline, bright crystalline laminated shale, and fractured shales, the resistance of nanopores

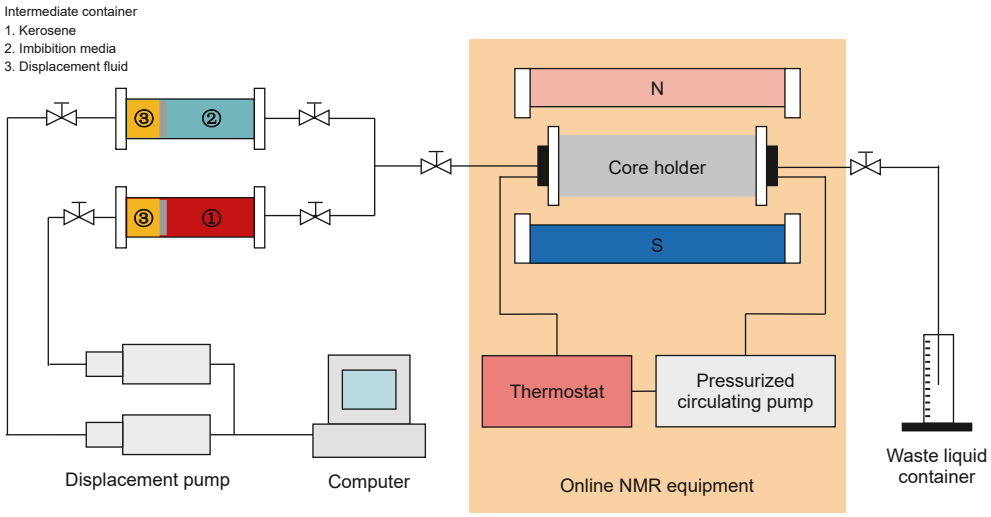


**Fig. 1.** The shale imbibition experimental equipment.

**Table 3**
Experiment parameters.

| No. | Key factor | Cores | Type of fluids | Pressure, MPa | Initial specific surface area, $m^{-1}$ | Wettability | Viscosity, mPa·s |
|---|---|---|---|---|---|---|---|
| 1 | Lithofacies | 7 | Deuterium oxide ($D_2O$) | Atmospheric | 2.43 | Neutral | 0.55 |
| | | 59 | $D_2O$ | Atmospheric | 2.40 | Neutral | 0.55 |
| | | 113 | $D_2O$ | Atmospheric | 2.41 | Neutral | 0.55 |
| | | 133 | $D_2O$ | Atmospheric | 2.43 | Neutral | 0.55 |
| 2 | Type of fluids/pressure | 70 | $D_2O$ | 0 | 2.39 | Neutral | 0.55 |
| | | 40 | $D_2O$ | 30 | 2.38 | Neutral | 0.55 |
| | | 25 | $D_2O$ with 0.1% FD-1 added | 30 | 2.40 | Neutral | 0.55 |
| | | 66 | $CO_2$ with $D_2O$ | 30 | 2.42 | Neutral | 0.55 |
| 3 | Fracture density | A | $D_2O$ | Atmospheric | 0.58 | / | 0.55 |
| | | B | $D_2O$ | Atmospheric | 0.51 | / | 0.55 |
| 4 | Wettability | 66 | $D_2O$ | Atmospheric | 2.38 | Oil-wet | 0.55 |
| | | 73 | $D_2O$ | Atmospheric | 2.40 | Neutral | 0.55 |
| | | 1 | $D_2O$ | Atmospheric | 2.41 | Hydrophilic 1 | 0.55 |
| | | 191 | $D_2O$ | Atmospheric | 2.40 | Hydrophilic 2 | 0.55 |
| 5 | Fluids viscosity | 11 | $D_2O$ | Atmospheric | 2.43 | Neutral | 0.55 |
| | | 34 | Slickwater with $D_2O$ | Atmospheric | 2.40 | Neutral | 1.70 |
| | | 49 | Low-viscosity fluid with $D_2O$ | Atmospheric | 2.42 | Neutral | 9.60 |
| | | 66 | Medium-viscosity fluid with $D_2O$ | Atmospheric | 2.41 | Neutral | 19 |
| | | 84 | High-viscosity fluid with $D_2O$ | Atmospheric | 2.40 | Neutral | 31 |
| | | 126 | Gel fluid with $D_2O$ | Atmospheric | 2.40 | Neutral | 52 |

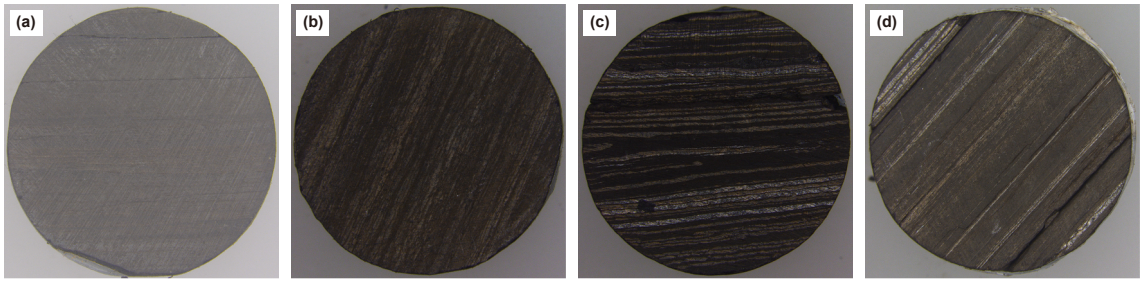


**Fig. 2.** Shale lithology of Jiyang Depression. **(a)** 59, massive shale; **(b)** 7, cryptocrystalline lamination shale; **(c)** 133, bright crystalline laminated shale; **(d)** 113, fractured shale.

is greater than that of micropores. Therefore, during the early stages of imbibition, these three types of shale primarily utilize oil stored in the larger pores. As the imbibition time extends, the nanopores begin to contribute to the oil supply.

### 3.2.2. Fluid types

Shale imbibition experiments are conducted using three different imbibition fluids, as shown in Table 3. The imbibition curves and shale samples recovery for each type of fluids are presented in Fig. 6, respectively. The imbibition equilibrium times for the four different imbibition fluids are 55, 168, 119, and 33 h for water (no pressure), water (with pressure), water with imbibition agent, and water added after pre-impregnation with $CO_2$, respectively. The slope of the imbibition curve effectively reflects the imbibition rate and reveals the imbibition performance. When the type of fluids is under pressure, in addition to capillary forces, the

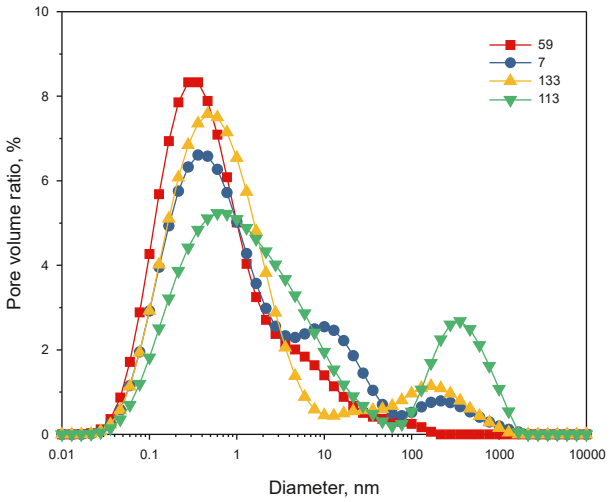


**Fig. 3.** Pore structure of shales.

pressure exerted on the medium also contributes to the imbibition drive, facilitating the imbibition process. As a result, the imbibition rate of a pressurized medium is faster than that of an unpressurized one. When the pressurized type of fluids contains imbibition agents that enhance the imbibition process, the imbibition rate is further increased. The pre-injected $CO_2$ encounters the oil phase in the shale, and since $CO_2$ can dissolve in crude oil to reduce its viscosity and improve its flowability, the imbibition rate of the system after adding water following $CO_2$ injection is faster.

The imbibition recovery results indicate that the best oil recovery is achieved when water is added after pre-impregnation with $CO_2$, with a core recovery of 26.6% (Fig. 6(b)). This is followed by the case where an imbibition agent is added to water, with a recovery of 20.6%. Next, water with applied pressure yields a recovery of 16.8%. The lowest recovery is observed when water without pressure is used as the type of fluids, with a core recovery of only 10.1%.

The contributions of pores of different scales to the recovery of shale oil during the imbibition process in different fluids are shown in Fig. 7. It can be observed that the four imbibition fluid mainly mobilize the crude oil within the nanopores and micro-nanopores. When water is used as the type of fluids, after pressurization, more crude oil within the submicropores can be recovered. However, the recovery of crude oil in the micro-nanopores is limited, and the crude oil within the micropores cannot be recovered through imbibition (Fig. 7(b)). After adding an imbibition agent to the water, the nanopores, micro-nanopores, and sub-micropores within the shale all contribute to a certain extent to the recovery. Moreover, when the imbibition time reaches 168 h, the crude oil in the micropores is mobilized (Fig. 7(c)). Imbibition with water after pre-injection of $CO_2$ enables the recovery of shale oil to reach a relatively high level within a short period (4 h), and during the later stages of pre-injection of $CO_2$ and

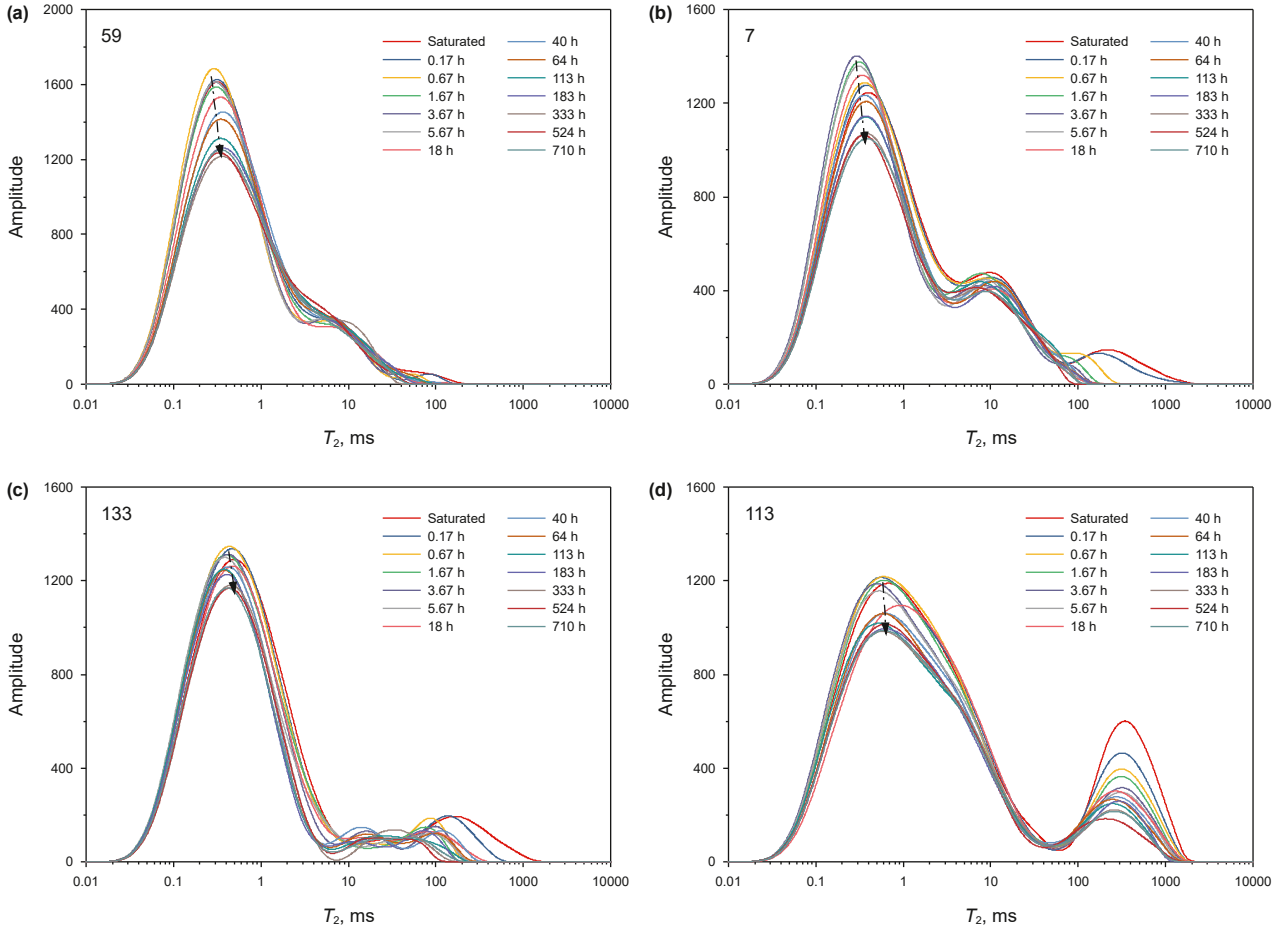


**Fig. 4.** The $T_2$ spectrum and imbibition recovery of four different samples. **(a)** 59 massive shale, **(b)** 7 cryptocrystalline laminated shale, **(c)** 133 bright crystalline laminated shale, **(d)** 113 fractured shale.

water addition, a small amount of crude oil in the micropores can be displaced through imbibition (Fig. 7(d)).

### 3.2.3. Fracture density

Fractures, serving as preferential pathways for fluid flow, have their distribution characteristics and quantity exerting a significant impact on fluid imbibition. The morphological changes of the internal fractures in core B under different imbibition times are shown in Fig. 8. It can be observed that as the soaking time of the shale increases, affected by the hydration effect, the clay minerals in the shale expand, resulting in the generation of microfractures within the shale. Firstly, fractures with larger

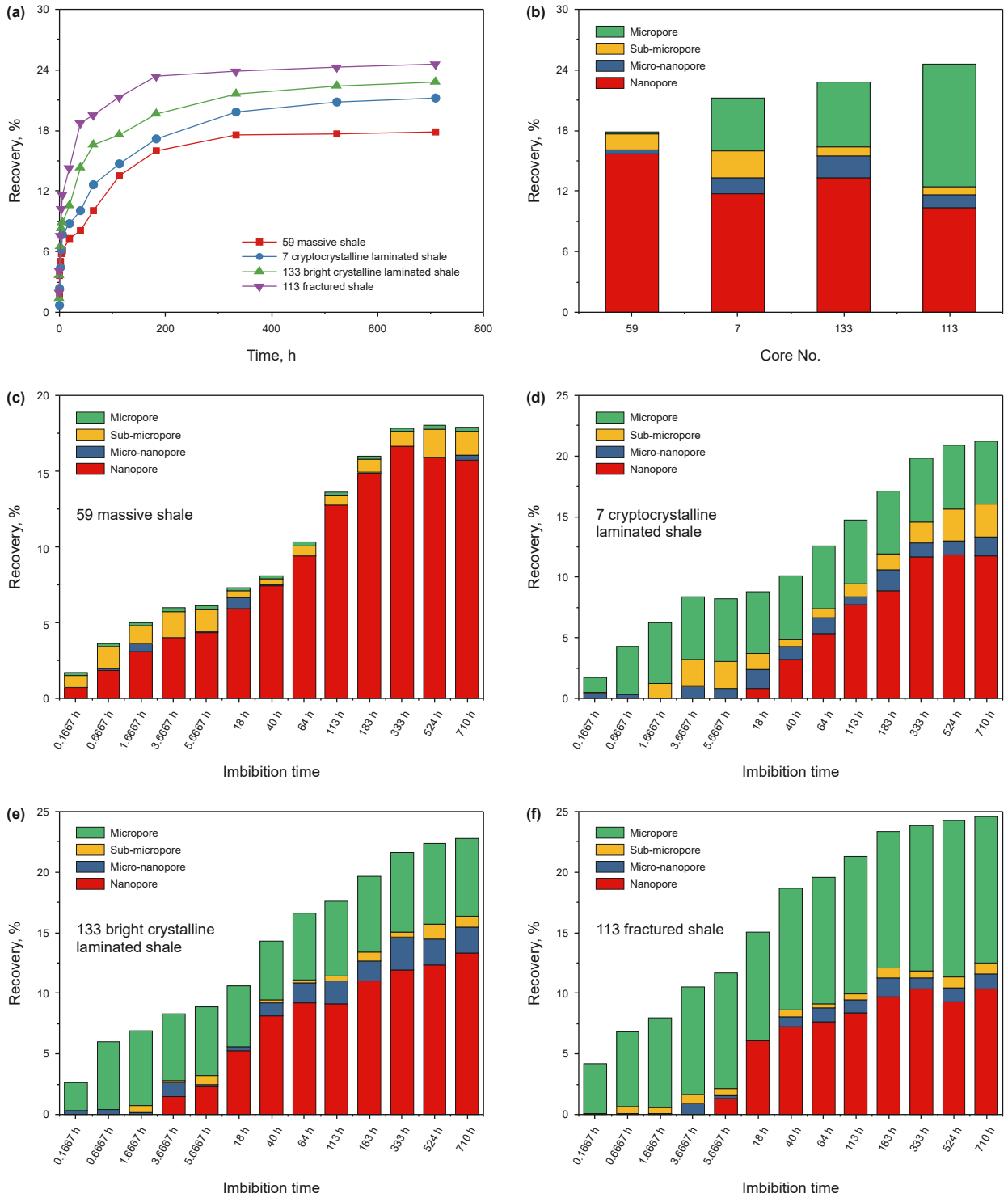


**Fig. 5.** Imbibition recovery. **(a)** Different lithology core imbibition curves, **(b)** oil recovery at 710 h of core imbibition. Oil recovery in different pores in four types shale at different imbibition times: **(c)** 59 massive shale, **(d)** 7 cryptocrystalline laminated shale, **(e)** 133 bright crystalline laminated shale, **(f)** 113 fractured shale.

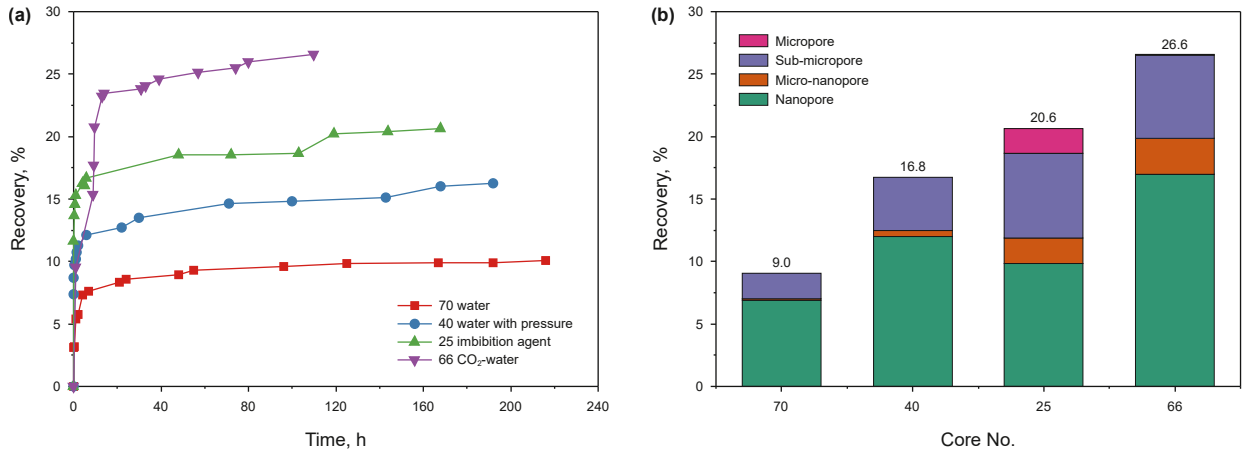


**Fig. 6.** Recovery of different type of fluids. **(a)** Imbibition curve of different imbibition media. **(b)** Recovery of different imbibition media.

apertures are formed in the laminar direction of the shale (Fig. 8 (b)). Subsequently, an irregular fracture appears perpendicular to the laminar direction (Fig. 8(c)). Eventually, when the imbibition time reaches 30 days, multiple fractures in the laminar direction of the shale successively increase in size and connect with each other, causing the destruction of the entire core structure. Simultaneously, this also increases the contact area between the shale matrix and the type of fluids.

The specific surface area variation in Core B during the imbibition process is presented in Fig. 9. The results indicate that before 191 h of imbibition, the specific surface area of Core B continuously increases from its initial value of 0.51 $m^2/m^3$ to 1.14 $m^2/m^3$, representing a 124% increase. However, between 191 and 768 h of imbibition, the specific surface area remains essentially unchanged.

The imbibition recovery degrees of core A and core B are shown in Fig. 10(a). Core A has no fractures inside, and its specific surface

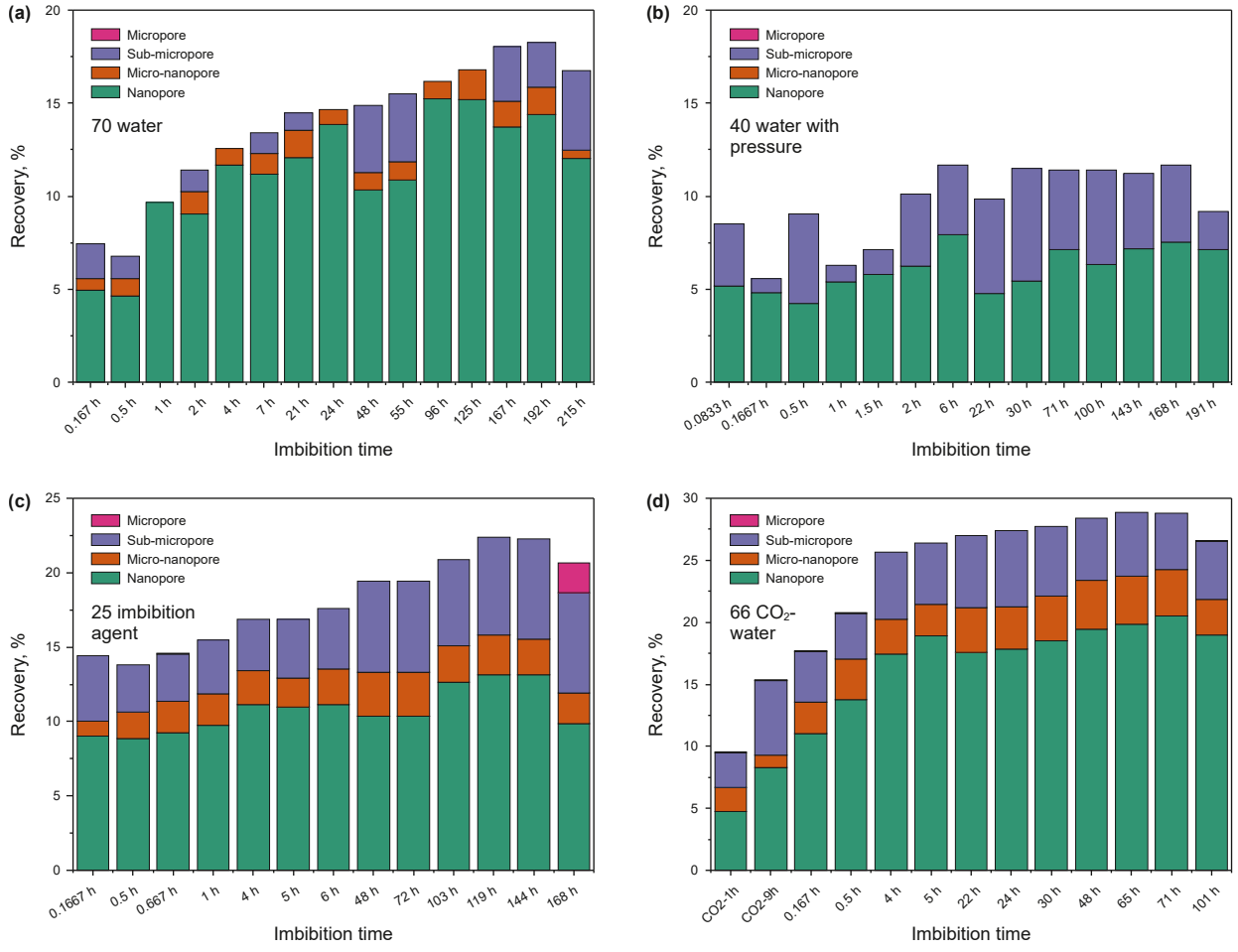


**Fig. 7.** Oil recovery in different sizes pores in shale with different imbibition media at different imbibition times: **(a)** 70, **(b)** 40, **(c)** 25, **(d)** 66.

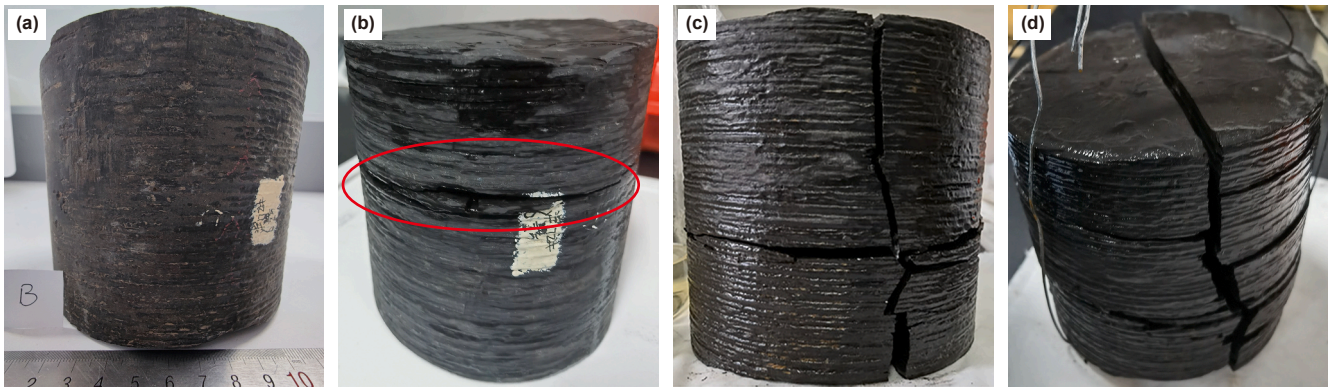


**Fig. 8.** Fracture configuration of core B under different imbibition periods: **(a)** initial; **(b)** imbibition 1 day; **(c)** imbibition 4 days; **(d)** imbibition 30 days.

area remains at 0.51 $m^2/m^3$ during the imbibition process. The change in the specific surface area of core B during the imbibition process is illustrated in Fig. 9. It can be observed that the change in the imbibition recovery rate of core B exhibits a consistent trend with the change in the specific surface area. When the fractures are in the expansion stage, the specific surface area increases rapidly, and the contact area between the type of fluids and the shale matrix expands, which is conducive to the imbibition of the shale, and the imbibition recovery rate also increases rapidly. When the change in the specific surface area of the fractures tends to reach equilibrium, the growth rate of the imbibition recovery slows down. Apparently, the fracture density of the core is a key factor restricting the imbibition displacement efficiency. After the imbibition time of both cores reaches 768 h, due to the opening of internal fractures, the specific surface area of core B is 2.24 times that of core A, and the imbibition recovery degree of core B is 46% higher than that of core A.

By comparing the recovery of different pores in core A and core B, it can be found that: for core A, the oil phase in the nanopores within the shale matrix is mainly drained, followed by that in the micro-nanopores, while the oil phase in the submicropores and micropores is hardly mobilized (Fig. 10(b)). For core B, the oil phase in the nanopores is also the main source of the recovered oil phase. However, due to the fractures and micropores generated in core B during the imbibition process, the type of fluids can more quickly reach the micropores along the microfractures, resulting in a significant contribution of the micropores to the overall recovery rate of core B (Fig. 10(c)).

#### 3.2.4. Wettability

Wettability plays a decisive role in the magnitude and direction of capillary forces during the imbibition process. The imbibition recovery and imbibition curves obtained from the imbibition experiments of four cores with different wettabilities are shown in Fig. 11, respectively. The results indicate that the imbibition displacement efficiency of water-wet cores is higher than that of neutrally-wet and oil-wet cores. In particular, the imbibition recovery of the oil-wet core is only 8.1%, which is merely 23.72% of the average imbibition recovery of water-wet cores (Fig. 11(a)). The more water-wet the core is, the faster the imbibition rate. The oil-wet core has the slowest imbibition rate (Fig. 11(b)). When the core is water-wet, the capillary force points from the type of fluids to the oil phase, serving as the driving force for the type of fluids to displace the oil phase. The stronger the water-wettability of the core, the greater the capillary force. Conversely, when the core is oil-wet, the capillary force becomes the resistance for the type of fluids to displace the oil phase, pointing from the oil phase to the type of fluids. The stronger the oil-wettability of the core, the more pronounced the resistance effect of the capillary force. Extending this conclusion to corresponding field conditions, it can be deduced that water-wet reservoirs have high imbibition displacement efficiency, as well as low water cut and low flowback rate.

#### 3.2.5. Viscosity

The imbibition recovery curves and recovery degrees of the cryptocrystalline laminated shale with different viscosity fluids, conducted as part of the imbibition experiments shown in Table 3, are presented in Fig. 12. The experimental results indicate that the imbibition recovery of water is lower than that of slickwater. However, as the fluid viscosity increases, the imbibition recovery continues to decrease, with high-viscosity fluids and gel solutions showing lower recovery than water. This suggests that increasing the viscosity of the fracturing fluid inhibits both imbibition displacement and fluid flow. From the perspective of imbibition-driven oil recovery, it is recommended to use slickwater-based fracturing fluids during hydraulic fracturing operations.

## 4. Discussion

### 4.1. Influencing factors of imbibition

#### 4.1.1. Porosity and permeability

The relationship between porosity, permeability, and spontaneous imbibition recovery in shale samples is illustrated by Fig. 13. As shown, both porosity and permeability exhibit weak correlations with recovery for the studied shale specimens. A very weak negative correlation is observed between porosity and recovery (Fig. 13(a), $R^2 = 0.066$), suggesting that although porosity to some extent reflects the storage capacity of the reservoir, its influence on the imbibition hydrocarbon recovery is limited. This may be attributed to the complex or heterogeneous pore structure that disrupts the capillary force-dominated imbibition process, rendering overall porosity insufficient to reliably determine imbibition efficiency.

Similarly, there is virtually no significant linear correlation between permeability and recovery (Fig. 13(b), $R^2 = 0.053$). This is likely because permeability typically represents the connectivity of macropores on a core scale, whereas imbibition often relies on transport through micro/nanopores, leading to a mismatch between the two parameters. While porosity and permeability are important petrophysical indicators for reservoir evaluation, they are not the dominant factors controlling shale imbibition recovery. In practice, the actual recovery efficiency is more likely governed by a combination of factors, including wettability variations, pore-throat structure, and fluid properties (such as viscosity and interfacial tension).

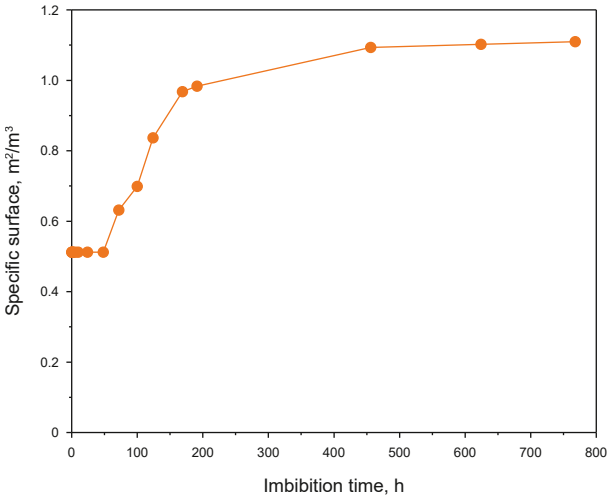


**Fig. 9.** Specific area of core B under different imbibition periods.

### 4.1.2. Wettability

The fitted relationship between overall wettability and imbibition recovery is depicted by Fig. 14(a). The results show that recovery significantly increases as wettability shifts toward a more water-wet state, exhibiting a strong positive correlation ($R^2 = 0.948$). This indicates that overall wettability is a key factor influencing spontaneous imbibition recovery. A more water-wet surface enhances the rock's affinity for the aqueous phase, thereby amplifying capillary driving forces and promoting the displacement of oil by water, leading to improved recovery efficiency. Fig. 14(b) shows a moderate positive correlation between micropore wettability and recovery ($R^2 = 0.402$), suggesting that although the correlation is weaker than that of overall wettability, micropore wettability still plays a meaningful role in the imbibition process. This is likely because capillary forces within micropores are relatively strong, allowing water to preferentially invade these smaller pores, enhancing displacement efficiency at the microscale. A weak correlation between macropore wettability and recovery is demonstrated by Fig. 14(c) ($R^2 = 0.068$), indicating that changes in macropore wettability have a limited effect on enhancing imbibition recovery. Due to the lower capillary pressure in larger pores, even a shift in wettability may not significantly improve water entry or flow. Moreover, macropores are generally less abundant in shale reservoirs, contributing less to the overall imbibition-driven recovery process.

### 4.1.3. Viscosity

A clear negative correlation between fluid viscosity and imbibition recovery is observed ($R^2 = 0.676$), as shown in Fig. 15. The trend indicates that as fluid viscosity increases, the imbibition recovery decreases accordingly. This result is closely related to the fundamental mechanism of spontaneous imbibition, which is primarily driven by capillary forces and strongly influenced by the resistance exerted by pore walls on fluid flow. Higher viscosity increases flow resistance, making it more difficult for the aqueous phase to enter the pore network under capillary force, thereby restricting the imbibition process and limiting the effective displacement and removal of oil, ultimately resulting in lower recovery efficiency. In addition, high-viscosity fluids may reduce interfacial mobility, making it more difficult for water molecules to displace oil molecules adsorbed onto pore surfaces. This further impedes spontaneous desorption and replacement at the fluid-solid interface. From an engineering perspective, fluid viscosity can be optimized to enhance imbibition efficiency through strategies such as selecting low-viscosity displacing agents, adjusting temperature, or introducing viscosity-reducing additives or surfactants. These approaches can significantly improve spontaneous imbibition recovery in unconventional reservoirs and provide theoretical guidance for the formulation of low-viscosity modified fluids for enhanced oil recovery applications.

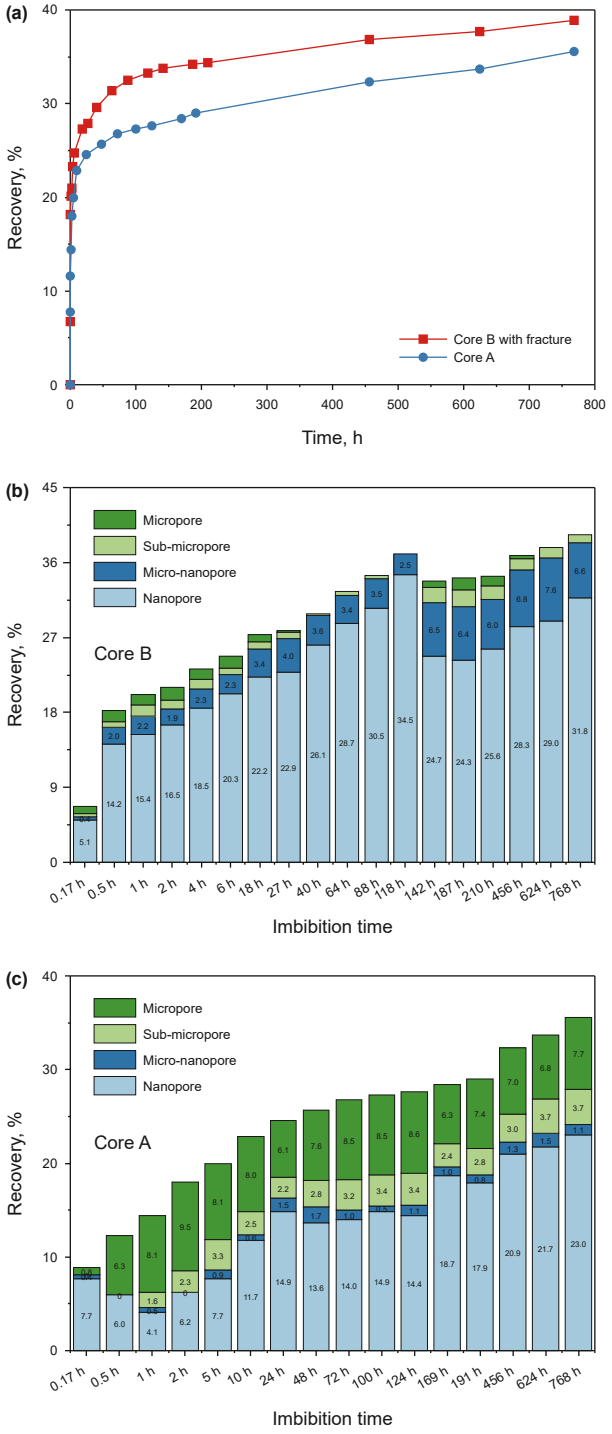


**Fig. 10.** Imbibition recovery of core A and core B.

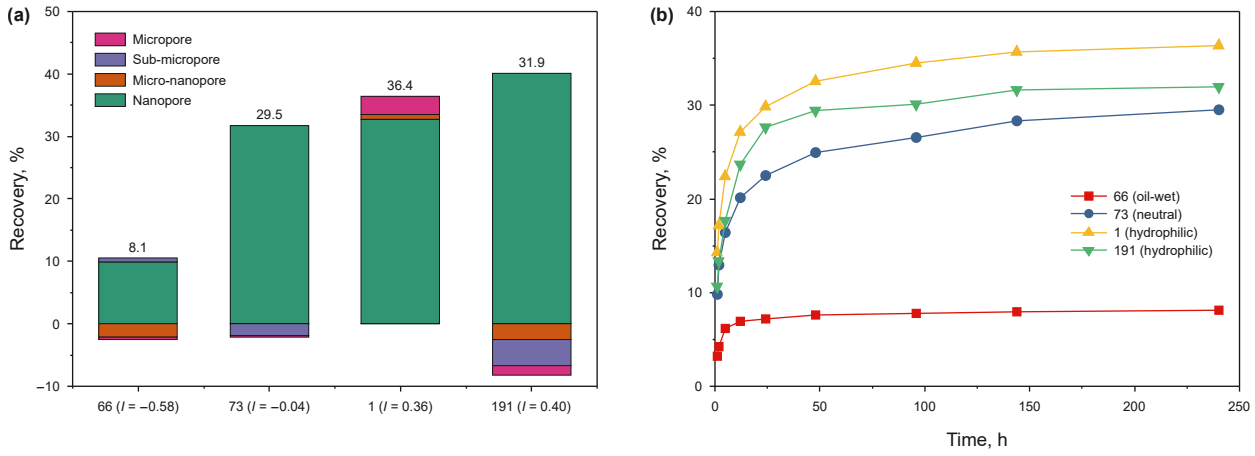


**Fig. 11.** Imbibition of shales with different wettability. **(a)** Oil imbibition recovery, **(b)** imbibition curves.

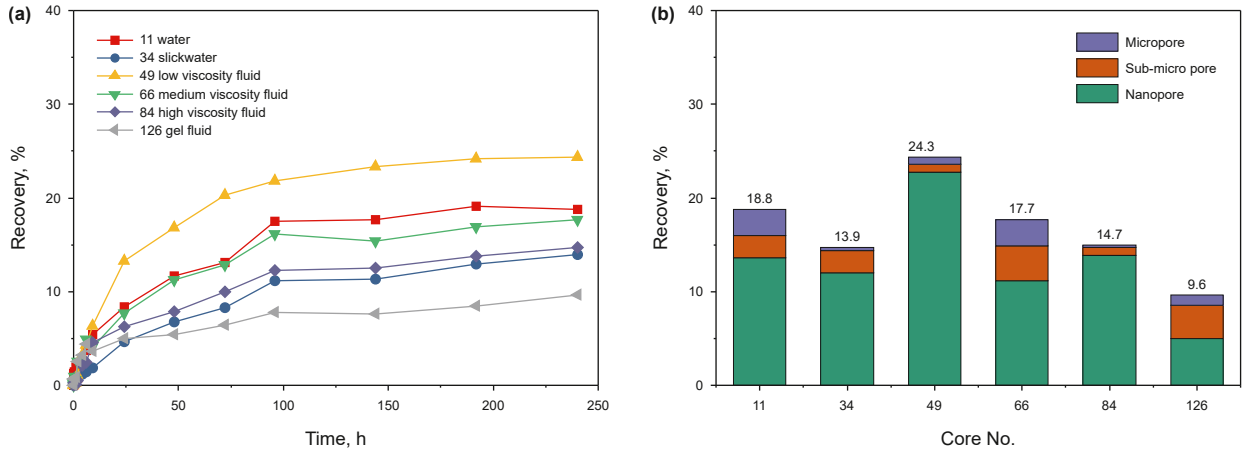


**Fig. 12.** Imbibition of fluids with different viscosities. **(a)** Imbibition curve, **(b)** recovery.

### 4.2. Summary of controls on imbibition recovery

The above analyses reveal that different reservoir and fluid properties exert distinct levels of influence on spontaneous imbibition recovery in shale. Porosity and permeability, while commonly used as fundamental petrophysical parameters, show only weak correlations with imbibition efficiency, indicating their limited predictive value in complex shale systems dominated by micro- and nanopore flow. In contrast, wettability demonstrates a strong positive correlation with recovery, especially when the rock surface becomes more water-wet, underscoring the crucial role of interfacial interactions and capillary forces. Micropore-scale wettability exerts a more pronounced effect than macropore wettability, highlighting the importance of pore-scale

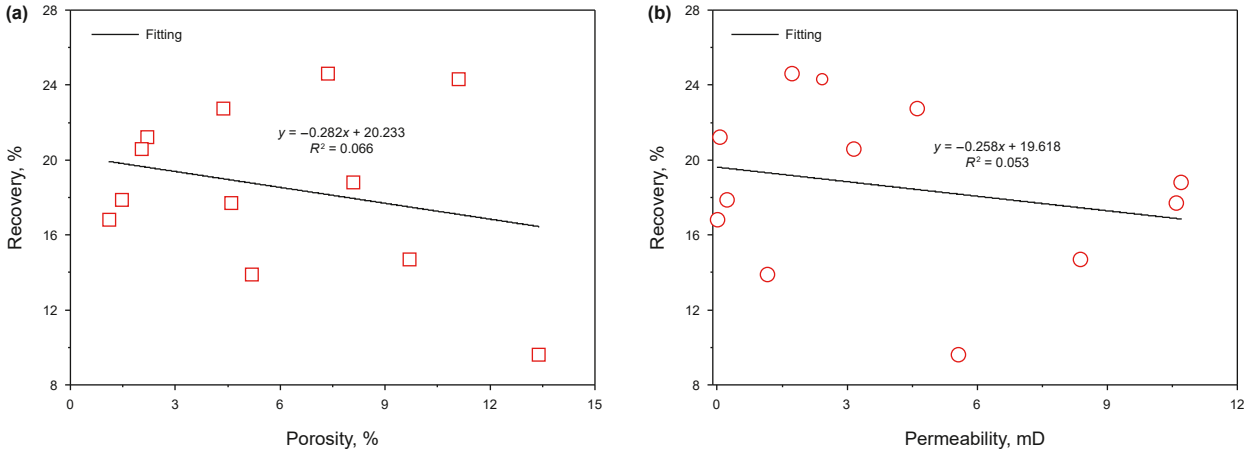


**Fig. 13.** The correlation between porosity, permeability, and imbibition recovery efficiency.

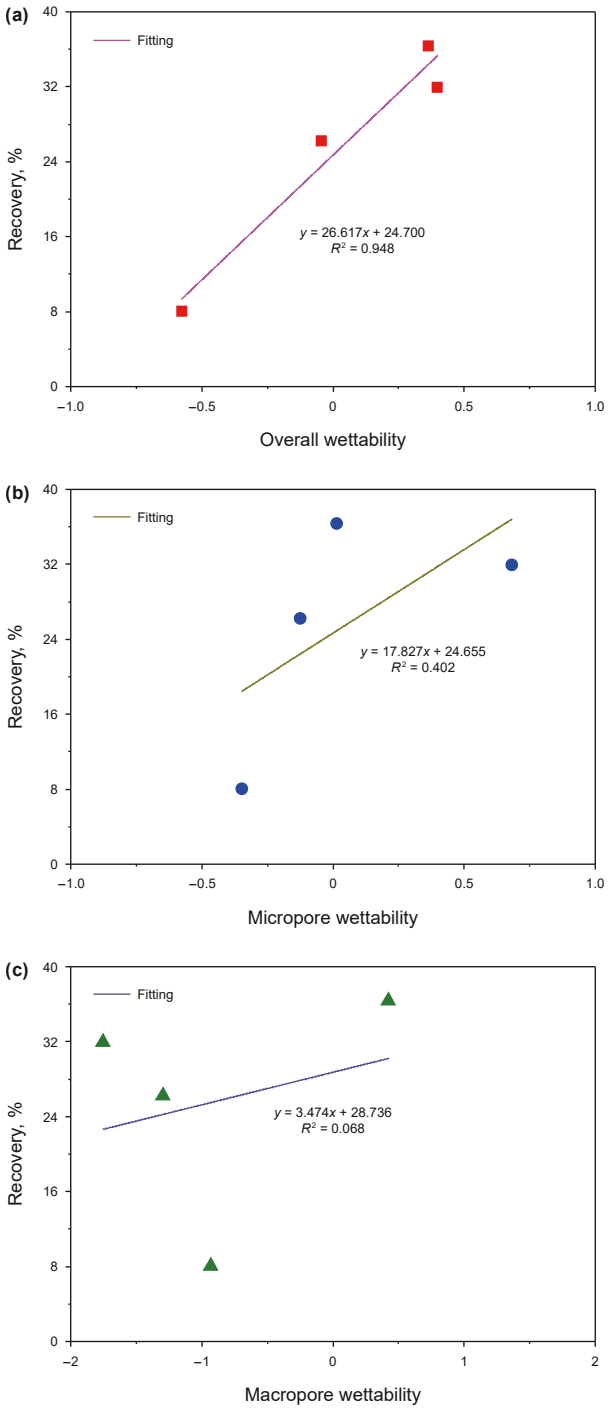


**Fig. 14.** The correlation between wettability and imbibition recovery.

heterogeneity (Fig. 16). Furthermore, fluid viscosity is shown to negatively impact imbibition efficiency, with higher viscosities impeding fluid entry and flow through fine pore networks due to increased resistance and reduced interfacial mobility. These findings collectively suggest that imbibition-driven oil recovery in shale is governed less by conventional macroscopic petrophysical properties and more by multiscale interfacial phenomena. Therefore, effective evaluation and enhancement of imbibition recovery in low-permeability reservoirs require an integrated approach that considers pore structure complexity, wettability behavior, and fluid characteristics.

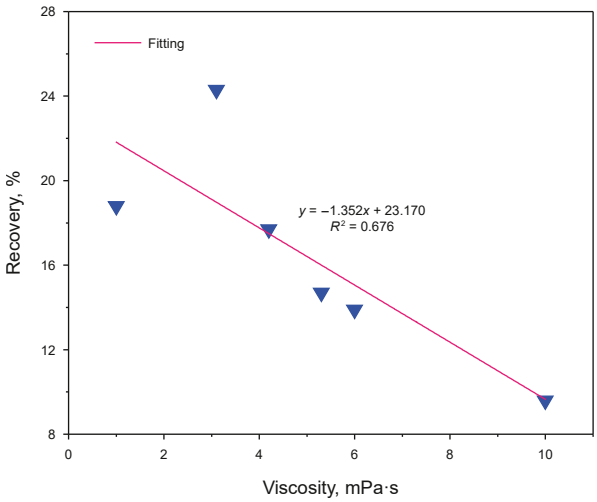


**Fig. 15.** The correlation between viscosity and imbibition recovery.

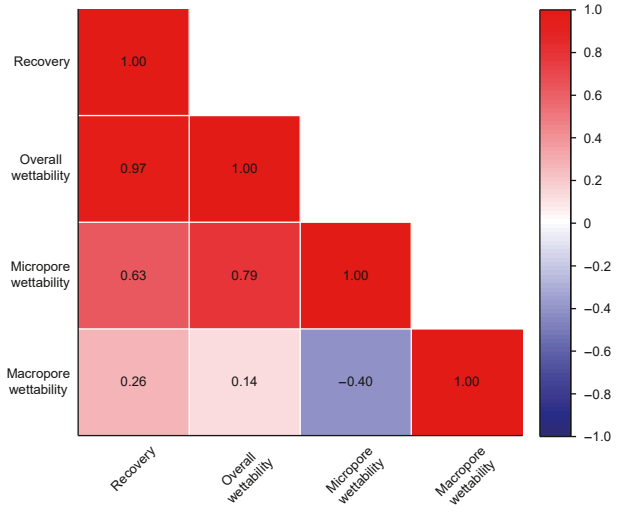


**Fig. 16.** Correlation between recovery and wettability in different pore scales.

## 5. Conclusion

In this study, imbibition experiments were conducted on shale oil samples from the Jiyang Depression using nuclear magnetic resonance techniques. The effects of various factors, including lithofacies type, type of fluids, fracture density, core wettability, and fluid viscosity, on shale imbibition behavior are systematically investigated. The main conclusions are as follows.

(1) The imbibition oil recovery of shale with lamination and microfractures is better than that of massive shale. Massive cores with few or no fractures mainly rely on the nanopores in the matrix for oil production. In contrast, cores with bedding planes and fractures preferentially utilize the larger pores, as the resistance in nanopores is higher than in micrometer-scale pores.

(2) The best imbibition oil recovery is achieved by pre-injecting $CO_2$ followed by water injection. This is followed by the addition of imbibition agents to water, then by water as the type of fluids under pressure, with the worst performance

being observed in conventional water injection at ambient pressure. Fractures increase the specific surface area of rocks, and shale with a higher fracture density shows significantly better imbibition oil recovery compared to shale with a lower fracture density.

(3) Water-wet cores exhibit significantly higher imbibition displacement efficiency than neutrally wet and oil-wet cores. Particularly, the imbibition recovery of oil-wet cores is only 23.72% of the average imbibition recovery of water-wet cores. Increasing the viscosity of the injected fluid inhibits both imbibition displacement and flow capacity.

(4) Wettability and fluid viscosity are identified as the key factors controlling spontaneous imbibition recovery, whereas porosity and permeability exhibit relatively weak correlations. Enhanced water-wetness significantly strengthens capillary driving forces, promoting more efficient displacement of oil by the aqueous phase and thereby improving recovery. In contrast, higher fluid viscosity increases flow resistance, hinders the imbibition process, and ultimately reduces recovery efficiency. Although porosity and permeability reflect the storage and flow capacity of the reservoir, their influence is limited in capillarity-dominated imbibition systems. Overall, the coordinated optimization of wettability and viscosity is more effective than relying solely on porosity–permeability parameters in enhancing oil recovery from shale reservoirs. These findings provide important theoretical guidance for the development of imbibition-based recovery technologies in unconventional reservoirs.

## CRediT authorship contribution statement

**Qi Lv:** Writing – original draft, Methodology, Investigation. **Jian Hou:** Writing – review & editing, Supervision. **Ting Chen:** Writing – review & editing, Formal analysis. **Yan-Feng Ji:** Writing – review & editing. **Jing Lv:** Writing – review & editing. **Jian-Xun Chen:** Writing – review & editing.

## Declaration of competing interest

The authors declare that they have no known competing financial interests or personal relationships that could have appeared to influence the work reported in this paper.

## Acknowledgments

This study was supported by the Joint Fund of the National Natural Science Foundation of China (No. U24B6002).

## References

Bai, G., Chen, G., Cai, Z., et al., 2025. Movable oil content evaluation in low-to-medium maturity lacustrine shale during in-situ conversion. Adv. Geo-Energy Res. 16 (1), 77–90. https://doi.org/10.46690/ager.2025.04.08.

Cai, J., Jin, T., Kou, J., et al., 2021. Lucas-Washburn equation-based modeling of capillary-driven flow in porous systems. Langmuir 37 (5), 1623–1636. https://doi.org/10.1021/acs.langmuir.0c03134.

Cai, J., Li, C., Song, K., et al., 2020. The influence of salinity and mineral components on spontaneous imbibition in tight sandstone. Fuel 269, 117087. https://doi.org/10.1016/j.fuel.2020.117087.

Cai, J., Qin, X., Wang, H., et al., 2025. Pore-scale investigation of forced imbibition in porous rocks through interface curvature and pore topology analysis. J. Rock Mech. Geotech. Eng. 17 (1), 245–257. https://doi.org/10.1016/j.jrmge.2024.02.047.

Chen, T., Yang, Z., Ding, Y., et al., 2018a. Waterflooding huff-n-puff in tight oil cores using online nuclear magnetic resonance. Energies 11 (6), 1524. https://doi.org/10.3390/en11061524.

Chen, T., Yang, Z., Luo, Y., et al., 2018b. Evaluation of displacement effects of different injection media in tight oil sandstone by online nuclear magnetic resonance. Energies 11 (10), 2836. https://doi.org/10.3390/en11102836.

Gao, Z., Hu, Q., 2016. Initial water saturation and imbibition fluid affect spontaneous imbibition into Barnett shale samples. J. Nat. Gas Sci. Eng. 34, 541–551. https://doi.org/10.1016/j.jngse.2016.07.038.

Ghanbari, E., Dehghanpour, H., 2015. Impact of rock fabric on water imbibition and salt diffusion in gas shales. Int. J. Coal Geol. 138, 55–67. https://doi.org/10.1016/j.coal.2014.11.003.

Gu, X., Pu, C., Huang, H., et al., 2017. Micro-influencing mechanism of permeability on spontaneous imbibition recovery for tight sandstone reservoirs. Petrol. Explor. Dev. 44 (6), 1003–1009. https://doi.org/10.1016/S1876-3804(17)30112-X.

Guo, J., Li, M., Chen, C., et al., 2020. Experimental investigation of spontaneous imbibition in tight sandstone reservoirs. J. Petrol. Sci. Eng. 193, 107395. https://doi.org/10.1016/j.petrol.2020.107395.

Han, X., Yu, H., Wu, Y., et al., 2025. Experimental investigation on the counter-current imbibition distance and factors influencing the imbibition recovery of carbonated fracturing fluid. SPE J. 30 (3), 1474–1491. https://doi.org/10.2118/218205-pa.

Kibria, M.G., Hu, Q., Liu, H., et al., 2018. Pore structure, wettability, and spontaneous imbibition of Woodford Shale, Permian Basin, West Texas. Mar. Petrol. Geol. 91, 735–748. https://doi.org/10.1016/j.marpetgeo.2018.02.001.

Li, S., Ye, Z., Wang, J., et al., 2023. Effects of fracturing fluid composition and other factors on improving the oil imbibition recovery of shale reservoir. Capillarity 9 (3), 45–54. https://doi.org/10.46690/capi.2023.12.01.

Liu, C., You, Q., Wang, T., et al., 2024. Study of microscopic imbibition and formation plugging mechanism of the compact oil reservoir based on sem and NMR analysis. Fuel 357, 129672. https://doi.org/10.1016/j.fuel.2023.129672.

Ma, Y., Deng, Z., Yue, J., et al., 2022. Nuclear magnetic resonance experiment on the influence of confining pressure on spontaneous imbibition of water in coal. Energy Fuels 36 (9), 4818–4829. https://doi.org/10.1021/acs.energyfuels.2c00177.

Meng, M., Ge, H., Ji, W., et al., 2015. Monitor the process of shale spontaneous imbibition in co-current and counter-current displacing gas by using low field nuclear magnetic resonance method. J. Nat. Gas Sci. Eng. 27, 336–345. https://doi.org/10.1016/j.jngse.2015.08.069.

Nie, X., Chen, J., 2018. Nuclear magnetic resonance measurement of oil and water distributions in spontaneous imbibition process in tight oil reservoirs. Energies 11 (11), 3114. https://doi.org/10.3390/en11113114.

Pranesh, V., 2018. Subsurface $CO_2$ storage estimation in bakken tight oil and eagle ford shale gas condensate reservoirs by retention mechanism. Fuel 215, 580–591. https://doi.org/10.1016/j.fuel.2017.11.049.

Roychaudhuri, B., Tsotsis, T.T., Jessen, K., 2013. An experimental investigation of spontaneous imbibition in gas shales. J. Petrol. Sci. Eng. 111, 87–97. https://doi.org/10.1016/j.petrol.2013.10.002.

Shao, X., Wang, K., Zhao, L., et al., 2024. Effects of salinity and driving pressure on water imbibition during shale formation. Capillarity 11 (3), 70–80. https://doi.org/10.46690/capi.2024.06.02.

Sun, L., He, W., Feng, Z., et al., 2022. Shale oil and gas generation process and pore fracture system evolution mechanisms of the continental Gulong Shale, Songliao Basin, China. Energy Fuels 36 (13), 6893–6905. https://doi.org/10.1021/acs.energyfuels.2c01407.

Tang, X., Jiang, S., Jiang, Z., et al., 2019. Heterogeneity of Paleozoic Wufeng-Longmaxi formation shale and its effects on the shale gas accumulation in the Upper Yangtze Region, China. Fuel 239, 387–402. https://doi.org/10.1016/j.fuel.2018.11.022.

Tangparitkul, S., Sukee, A., Jiang, J., et al., 2023. Role of interfacial tension on wettability-controlled fluid displacement in porous rock: A capillary-dominated flow and how to control it. Capillarity 9 (3), 55–64. https://doi.org/10.46690/capi.2023.12.02.

Wang, L., Liu, B., Bai, L., et al., 2024. Pore evolution modeling in natural lacustrine shale influenced by mineral composition: Implications for shale oil exploration and $CO_2$ storage. Adv. Geo-Energy Res. 13 (3), 218–230. https://doi.org/10.46690/ager.2024.09.07.

Wang, W., Xie, Q., Wang, H., et al., 2023. Pseudopotential-based multiple-relaxation-time lattice Boltzmann model for multicomponent and multiphase slip flow. Adv. Geo-Energy Res. 9 (2), 106–116. https://doi.org/10.46690/ager.2023.08.04.

Wang, X., Hou, J., Li, S., et al., 2020. Insight into the nanoscale pore structure of organic-rich shales in the Bakken formation, USA. J. Petrol. Sci. Eng. 191, 107182. https://doi.org/10.1016/j.petrol.2020.107182.

Wei, J., Shang, D., Zhao, X., et al., 2024. Experimental study on production characteristics and enhanced oil recovery during imbibition and huff-n-puff injection in shale reservoir. Capillarity 12 (2), 41–56. https://doi.org/10.46690/capi.2024.08.02.

Xia, X., Xia, Y., Zhao, F., et al., 2024. Evaluating the surface relaxivity and movable fluid of low-permeability sandstones based on low-field nuclear magnetic resonance. Phys. Fluids 36 (11), 116619. https://doi.org/10.1063/5.0238003.

Xiao, W., Yang, Y., Bernabé, Y., et al., 2023. Experimental study on EOR in shale oil cores during associated gasflooding: A case study from Yanchang formation, Ordos Basin. SPE J. 28 (5), 2329–2345. https://doi.org/10.2118/214704-pa.

Xiao, Y., You, Z., Du, Z., et al., 2024. Review on spontaneous imbibition mechanisms in gas-water systems: Impacts on unconventional gas production and $CO_2$ geo--sequestration. Gas Sci. Eng. 131, 205466. https://doi.org/10.1016/j.jgsce.2024.205466.

Yan, G., Qin, Z., Marsh, S., et al., 2021. Nanopore size distribution heterogeneity of organic-rich shale reservoirs using multifractal analysis and its influence on porosity–permeability variation. Energy Fuels 35 (17), 13700–13711. https://doi.org/10.1021/acs.energyfuels.1c01654.

Yang, L., Wang, H., Xu, H., et al., 2023a. Experimental study on characteristics of water imbibition and ion diffusion in shale reservoirs. Geoenergy Sci. Eng. 229, 212167. https://doi.org/10.1016/j.geoen.2023.212167.

Yang, R., Hu, Q., Yi, J., et al., 2019. The effects of mineral composition, TOC content and pore structure on spontaneous imbibition in lower Jurassic Dongyuemiao shale reservoirs. Mar. Petrol. Geol. 109, 268–278. https://doi.org/10.1016/j.marpetgeo.2019.06.003.

Yang, Y., Wang, S., Feng, Q., et al., 2023b. Imbibition mechanisms of fracturing fluid in shale oil formation: A review from the multiscale perspective. Energy Fuels 37 (14), 9822–9840. https://doi.org/10.1021/acs.energyfuels.3c00502.

Zhang, C., Liu, D.-D., Jiang, Z.-X., et al., 2022. Mechanism for the formation of natural fractures and their effects on shale oil accumulation in Junggar Basin, NW China. Int. J. Coal Geol. 254, 103973. https://doi.org/10.1016/j.coal.2022.103973.

Zhang, J., 2016. Experimental study and modeling for $CO_2$ diffusion in coals with different particle sizes: Based on gas absorption (imbibition) and pore structure. Energy Fuels 30 (1), 531–543. https://doi.org/10.1021/acs.energyfuels.5b02546.

Zhao, H., Hu, J., Wang, J., et al., 2019. A comprehensive model for calculating relative permeability based on spontaneous imbibition and CT scanning measurement. Fuel 247, 287–293. https://doi.org/10.1016/j.fuel.2019.03.056.

Zou, C., Yang, Z., Cui, J., et al., 2013. Formation mechanism, geological characteristics and development strategy of nonmarine shale oil in China. Petrol. Explor. Dev. 40 (1), 15–27. https://doi.org/10.1016/s1876-3804(13)60002-6.

Zou, Y.R., Sun, J.N., Li, Z., et al., 2018. Evaluating shale oil in the Dongying Depression, Bohai Bay Basin, China, using the oversaturation zone method. J. Petrol. Sci. Eng. 161, 291–301. https://doi.org/10.1016/j.petrol.2017.11.059.